Formation of Active Sites for Oxygen Reduction Reactions by Transformation of Nitrogen Functionalities in Nitrogen-Doped Carbon Nanotubes

Tiva Sharifi, Guangzhi Hu, Xueen Jia, and Thomas Wågberg*

Department of Physics, Umeå University, S-901 87 Umeå, Sweden

ABSTRACT Heat treating nitrogen-doped multiwalled carbon nanotubes containing up to six different types of nitrogen functionalities transforms particular nitrogen functionalities into other types which are more catalytically active toward oxygen reduction reactions (ORR).

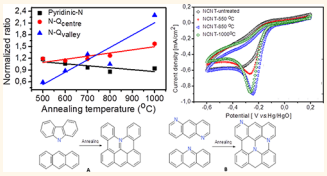

In the first stage, the unstable pyrrolic functionalities transform into pyridinic functionalities followed by an immediate transition into quaternary center and valley nitrogen functionalities. By measuring the electrocatalytic oxidation reduction current for the different samples, we achieve information on the catalytic activity connected to each type of nitrogen functionality. Through this, we conclude that quaternary nitrogen valley sites, N-Q_{valley}, are the most active sites for ORR in N-CNTs. The number of electrons transferred in the ORR is determined from ring disk electrode and rotating ring disk electrode measurements. Our measurements indicate that the ORR processes proceed by a direct four-electron pathway for the N-Q_{valley} and the pyridinic sites while it proceeds by an indirect two-electron pathway *via* hydrogen peroxide at the N-Q_{center} sites. Our study gives both insights on the mechanism of ORR on different nitrogen functionalities in nitrogen-doped carbon nanostructures and it proposes how to treat samples to maximize the catalytic efficiency of such samples.

KEYWORDS: nitrogen-doped carbon nanotubes · nitrogen functionalities · X-ray photoelectron spectroscopy · electrochemistry · cyclic voltammetry · oxygen reduction reactions

Carbon nanotubes and carbon fibers are attractive due to their excellent properties as support for metal nanoparticle catalysts leading to highly efficient composite materials for various kinds of electrochemical applications.[1−4] Recently, the intrinsic catalytic properties of nonmetallic nitrogen-doped multiwalled carbon nanotubes (N-CNTs) have received increasing attention as oxygen reduction reaction (ORR) catalysts. This is not only due to the potentially low cost and high abundance of metallic free catalysts but also due to their better stability toward CO poisoning compared to traditional platinum catalysts.[5−9] The role of nitrogen doping in carbon nanostructures for catalytic oxidation reactions has been frequently debated. It is clear that the inclusion of nitrogen in the honeycomb carbon structure induces active sites that can participate in breaking the O−O bonds of oxygen molecules. To achieve high turnover numbers for oxygen reduction reactions, it is important that the active sites exhibit a relatively low binding energy for the oxygen but yet a high electron density localized around the active catalytic site.[5,10] The high ORR electrocatalytic activity in N-doped multiwalled carbon nanotubes is rationalized by an appropriate balance of these two properties.[5] Consequently, Chen *et al.*[11] and Maldonado *et al.*[12] reported a strong correlation between oxygen reduction current and the nitrogen dopant level in N-CNTs and in N-doped carbon fibers, respectively. However, although the basic mechanisms of ORR in nitrogen-doped nanostructures are known, there is still a large controversy, both regarding the catalytic efficiency of different nitrogen functionalities and the role of metallic impurities present in the samples. Kundu *et al.*[13] reported that pyridinic type of nitrogen functionalities are the most catalytically active site for ORR in accordance with a study by Rao *et al.*[14] In contrast, Niwa *et al.*[15] found that N-CNTs with a comparably larger amount of graphitic nitrogen exhibit a higher ORR electrocatalytic activity than those containing a large amount of pyridinic nitrogen. A recent report on N-doped graphene partly supports the results of Niwa *et al.* but also concludes that the pyridinic sites lower the ORR onset potential.[16] Nitrogen doping level and

* Address correspondence to thomas.wagberg@physics.umu.se.

Received for review June 29, 2012 and accepted September 28, 2012.

Published online September 28, 2012
10.1021/nn302906r

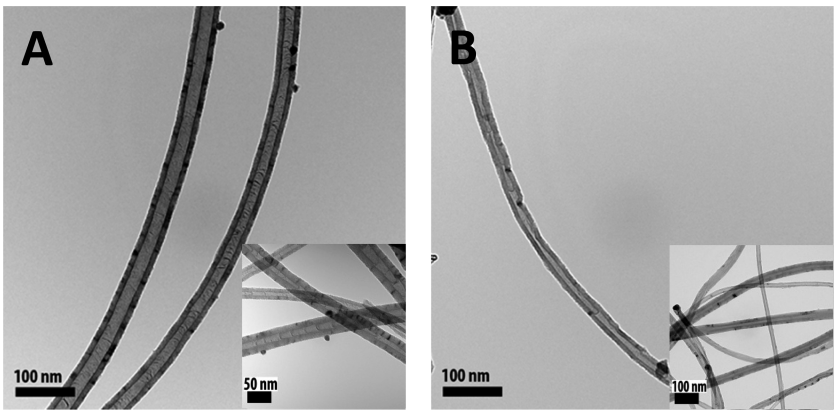

Figure 1. TEM images of (A) N-CNTs and (B) CNTs grown at 800 °C with FCCVD method.

type of nitrogen functionalities depend strongly on synthesis conditions[17−20] and are in general not easily controlled. Most studies so far have therefore studied samples synthesized at different conditions which contain various nitrogen functionalities. However, in such set of samples, hidden parameters, such as tube length, tube diameter, and number of walls, might have an impact on catalytic properties without being considered.

In this study, we have therefore used another approach to reveal and gain more knowledge on the role of nitrogen functionalities in N-CNTs for ORR. Instead of trying to control the type of nitrogen functionalities in the growth process, we have focused on transforming the nitrogen functionalities into other types in the already synthesized samples. Similar procedures have been used to study nontubular nitrogen-containing carbon materials.[21] We show that by heat treating samples containing up to six different types of nitrogen functionalities, it is possible to transform particular types of nitrogen into other types of functionalities which are more catalytically active toward ORR. By measuring the electrocatalytic oxidation reduction current density, the ORR onset potential, and the ORR electron transfer number for the different samples, we achieve information on the catalytic ORR process connected to each type of nitrogen functionality. We conclude that quaternary nitrogen valley sites, N-Q_{valley}, are the most active sites for ORR in N-CNTs in agreement with theoretical predictions,[22] which is more active than pyridinic nitrogen and N-Q_{center} (usually referred as graphitic nitrogen) sites. The pyridinic nitrogen functionalities on the other hand seem to lower the onset potential, in agreement with the study by Lai *et al.*[16] The number of transferred electrons, determined from rotating disk electrode and rotating ring disk electrode measurements, indicates a four-electron pathway for the edge states, N-Q_{valley}, and pyridinic while they indicate a two-electron pathway for the N-Q_{center} sites. Our study gives insights on the ORR mechanism on different nitrogen functionalities in nitrogen-doped carbon nanostructures and demonstrates how to treat samples to maximize the catalytic efficiency of such samples.

RESULTS AND DISCUSSION

Nondoped and nitrogen-doped CNTs were synthesized by floating catalyst CVD method using ferrocene (catalyst precursor), either pyridine (C/N precursor) or acetylene (C precursor), and argon (carrier gas). After the growth, CNTs were collected from the walls of the quartz tube (approximately 30 mg in each run). Four samples were produced at roughly similar conditions containing 3−6% of nitrogen. The samples were annealed in argon by loading them in an aluminum oxide crucible and placed at the center of a furnace. The system was purged with argon (162 mL/min), heated to desired temperature, treated at the predefined time, and then cooled to room temperature. All samples were characterized before and after the heat treatments by X-ray photoelectron spectroscopy (XPS) and various electrochemical methods.

Figure 1 shows TEM images of N-CNTs or CNTs and illustrates the difference in morphology between N-doped and nondoped CNTs. The outer diameter is about 20 nm for the nondoped tubes, whereas it is about 30 nm for the N-doped tubes. The large number of black regions have been analyzed in detail, and we note that these regions are not iron-rich but rather represent highly defective regions in the N-CNTs, most probably due to the presence of nitrogen (Supporting Information, Figure S1).[17]

Figure 2A,B shows typical XPS spectra for N-CNTs. The low-resolution spectrum (Figure 2A) displays a strong C 1s signal at 284.6 eV together with a N 1s signal from nitrogen at ∼401 eV and an O 1s signal at ∼531 eV. A typical high-resolution N 1s spectrum of the N-CNTs is shown in Figure 2B. Generally, the synthesized samples contain up to six different nitrogen functionalities. The different chemical states of nitrogen are represented by six main peaks in the N 1s high-resolution spectrum centered at 398.6−398.8 eV (N 1), 400.3 eV (N 2), 401 eV

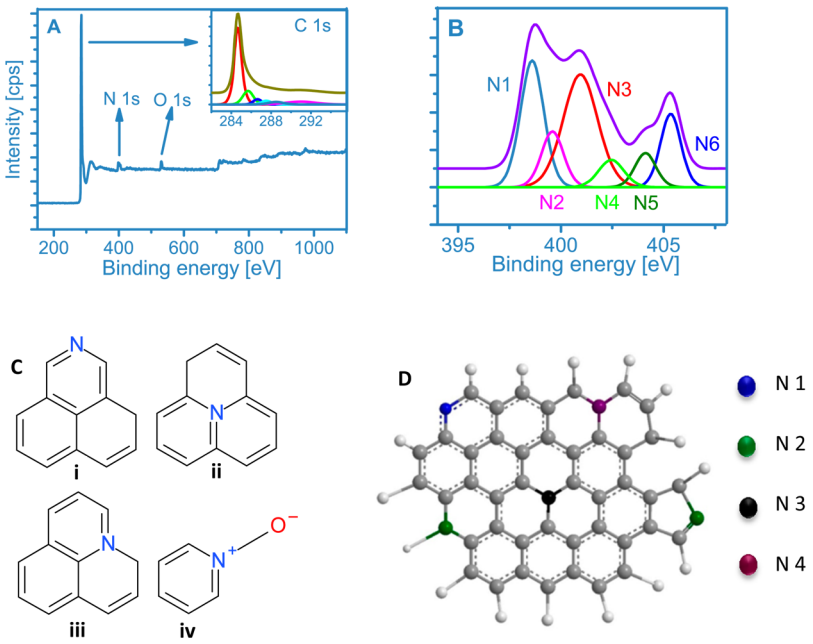

Figure 2. (A) Typical XPS spectrum of nitrogen-doped CNTs with assigned peaks. Inset: high-resolution C 1s peak, (B) high-resolution N 1s peak, (C) possible nitrogen positions in the structure; (i) top-N, (ii) center-N, (iii) valley-N, and (iv) oxide-N. (D) Different nitrogen functionalities in a graphitic sheet.

(N 3), 402.3−402.6 eV (N 4), 403.8−404.1 eV (N 5), and 405.3 eV (N 6).

The interpretation and assignment of nitrogen-doped carbon nanostructures is not straightforward and depends on a number of factors as discussed by Pels *et al.*, who combined model calculations with a study of nitrogen functionalities in carbon coals.[23] A more positively charged atom needs more energy to release an electron. The electron density of nitrogen atoms incorporated into a graphitic framework strongly depends on the local structure, and hence the binding energy probed by XPS reveals important information on the chemical states of nitrogen functionalities. Charge calculations[24,25] show that the positive charge on the nitrogen atoms in the four different configurations shown in Figure 2C increases from i to iv (and from N 1 to N 4 in Figure 2D), in good agreement with the measured binding energy for these N−C bonds.[23]

The least positively charged nitrogen displayed in Figure 2C (i) and Figure 2D (N 1) corresponds to pyridinc-N. Pyridinic-N refers to nitrogen atoms which contribute to the π-system with one p-electron and are represented by a well-defined peak at the binding energy of ~398.6 eV in nitrogen-containing carbonaceous materials (Figure 2B).[26] Pyrrolic type of nitrogen contributes to the π-system with two p-electrons and hence has higher binding energy of about 400.3 eV (N 2). The difference between pyridinic and pyrrolic nitrogen configurations in a graphene sheet is illustrated in Figure 2D. At the edges of a graphene layer, substitution of C−H by N leads to pyridinic nitrogen, whereas substitution of C by N either in a six-membered ring or a five-membered ring leads to pyrrolic nitrogen.[27]

The identification of other peaks is less ambiguous and still under debate, although the analysis of model compounds has helped to clarify their identification.[23] Quaternary nitrogen (N-Q) constitutes the most complicated assignment. It is represented in the N 1s spectra by a broad peak centered on 401.3 eV with a FWHM of about 3 eV. The large FWHM signals that the peak should be assigned to more than one nitrogen functionality. Wang *et al.*[28] suggested that N-Q represents nitrogen incorporated into a graphene layer at a position other than pyridinic-N. By reviewing a large number of explanations, Buckley[29] concluded that N-Q is either protonated pyridinic-N or pyridinic-*N*-oxide. On the other hand, in nitrogen-doped CNTs, nitrogen oxide functionalities are usually assigned by peaks positioned between 402 and 405 eV,[30] which contradicts the conclusion by Buckley *et al.*[29] The assignment of N-Q to non-oxide nitrogen functionalities is further supported by the presence of N-Q functionalities in nitrogen-containing petroleum fuel cokes after calcination at high temperature.[31] Since nitrogen oxide functionalities exhibit low thermal stability, this indicates that N-Q should not be assigned to pyridinic-*N*-oxide, which is in very good agreement with our observations discussed below. Instead, the double assignment to N-Q functionalities can be well explained by calculations done by Pels *et al.*[23] Accordingly, the center-N (N 3) displayed in Figure 2C (ii) is slightly less positively charged than valley-N (N 4) shown in Figure 2C (iii). This gives rise to a shift in binding energy from 401 eV for center-N to 402.3 eV for valley-N. A plausible assignment is therefore that N-Q functionalities are represented by two peaks, one

around 401 eV that is typically referred to as graphitic nitrogen and here denoted as N-Q_{center} (N 3)[32,33] and one around 402.3−402.6 eV which we refer to as N-Q_{valley} (N 4). Nitrogen functionalities with higher binding energies in the XPS spectra (N 5 and N 6) are assigned to nitrogen oxide groups.

In our study, we have investigated samples which intentionally contained a large diversity of nitrogen functionalities. Our aim is to understand and ultimately control how these nitrogen functionalities evolve by thermal treatment and simultaneously investigate how the ORR activity correlates to the different types of nitrogen functionalities.

A typical as-synthesized N-CNT sample before any thermal treatment has a distribution of nitrogen functionalities which determined from XPS measurements contain pyridinic (34%), pyrrolic (9%), N-Q_{center} (36%), and N-Q_{valley} (13%) nitrogen functionalities and a remaining fraction of different nitrogen oxide groups (8%). However, in order to be able to analyze the response to thermal treatment of nitrogen functionalities in a large number of samples with different starting N/(C + N) ratios, we have normalized the measurements to each chemical state of nitrogen in the original sample before thermal treatment as explained by eq 1

$$\frac{I(\mathrm{N1s})_{\text{specific N functionality of sample } i \text{ treatment at temperature } T}}{I(\mathrm{N1s})_{\text{specific N functionality of sample } i \text{ before treatment}}} \quad (1)$$

where the I(N 1s) is the integrated area obtained from the deconvolution of the XPS N 1s signal for the specific chemical state of nitrogen after normalization to the N/(C + N) ratio. Figure 3 presents the evolution of the different types of nitrogen functionalities by analyzing in total 24 samples treated at temperatures between 500 and 1000 °C in argon. In addition to the evolutions shown in Figure 3, which will be discussed in detail below, we make two important observations in our data: (i) The peaks related to certain types of nitrogen oxide groups (N 5 and N 6) rapidly vanish already by the thermal treatment at 500 °C. The disappearance of certain nitrogen oxide groups is accompanied by a concomitant decrease of the O 1s peak. Concurrent with the decrease of the O 1s peak and the N 5 and N 6 peaks, we observe that the peaks related to quaternary nitrogen, N-Q_{center} and N-Q_{valley}, increase. This confirms the non-oxygen-related nature of the N-Q peaks and supports the theoretical calculations.[23] (ii) Pyrrolic-N (N 2) rapidly decreases upon thermal annealing. It is still observable in the samples annealed up to 500 °C but disappears completely after annealing at higher temperatures. The decrease in pyrrolic-N functionalities at high temperatures is in agreement with earlier reports on thermal treatment of nitrogen-containing chars,[21] but the decrease occurs at lower temperatures than in the chars where the pyrrolic-N functionalities show a rather good stability up to 1000 °C.[23] Our observations of a fast decrease in pyrrolic-N and a slow decrease in pyridinic-N concurrent with a rapid increase in quaternary nitrogen, N-Qs, can be rationalized by two different models. The first "ring expansion" model represents a route for the transformation of pyrrolic-N (N 2) to pyridinic-N (N 1) and N-Qs (N-Q_{center} and N-Q_{valley}).[34] However, the gradual decrease of pyridinic-N at higher temperatures also signals a transformation of pyridinic-N to N-Qs and can be well described by the model of Pels *et al.* shown in Figure 4A,B.

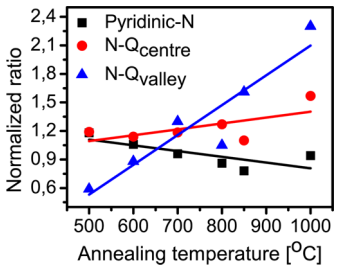

Figure 3. Normalized ratio of nitrogen functionalities calculated from eq 1 *vs* annealing temperature.

Our results indicate that pyridinic-N functionalities are more stable than pyrrolic-N but that both are transformed to N-Qs when a sufficient temperature is provided. This agrees with previous reports for nitrogen-containing carbon structures,[21,35−37] although in most reports, the experimental trend is not as clear as in our data. It is interesting to note though that, in a related report by Kundu *et al.*,[13] no significant transformation of nitrogen functionalities was observed up to 720 °C. Although their investigated annealing temperatures are lower, the different behavior indicates that small differences in N-CNT properties might influence the stability of nitrogen functionalities. Our data show that surface rearrangement is more efficient at high temperatures and converts the original material

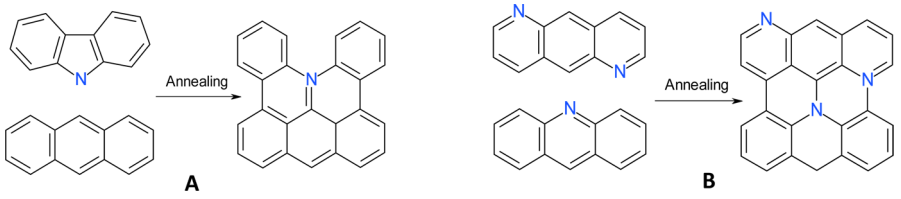

Figure 4. Condensation reactions by annealing (A) from pyrrolic-N (N 2) to N-Q_{valley} (N 4) and (B) from pyridinic-N (N 1) to N-Qs (N-Q_{center} and N-Q_{valley}).

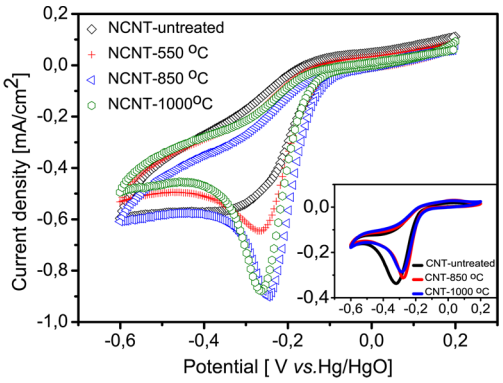

Figure 5. Background-corrected cyclic voltammograms in oxygen-saturated 1 M KOH electrolyte for undoped CNTs and nitrogen-doped CNTs annealed at high temperatures.

to a sample containing more N-Qs. After thermal annealing at 1000 °C, the ratio of N-Q_{valley} is almost 2.5 times higher than that in the starting material.

Figure 5 shows the electrocatalytic performance for CNTs (inset) and N-CNTs toward ORR. When the alkaline solution was purged with nitrogen, no redox peak is observed for either the CNTs or the N-CNTs in the potential window between −0.6 and 0.2 V. When instead purging the solution with oxygen, a broad reduction peak was observed at the CNT-modified electrode.

The thermal annealing of the CNT samples removes impurities and heals out defects. A comparison of the Raman spectra of an untreated CNT sample and a sample heat treated at 850 °C shows that the I_D/I_G of untreated CNTs (0.997) is significantly larger than the I_D/I_G of treated CNTs at 850 °C (0.811) (see Figure S2, Supporting Information). The I_D/I_G ratio is a very direct measure of the amount of defect in carbonaceous materials,[38] which supports our interpretation that defects are healed out during the annealing of the CNTs. The lower number of defects enhances the electron transfer properties and causes a positive shift of the reduction potential (inset, Figure 5). Simultaneously, the decreased number of defects by thermal treatment reduces the number of available catalytically active sites, which rationalizes the slight decrease in ORR current density. Values for current density and reduction peak potential are summarized in Tables S1 and S2. In total, it is clear from our results that the thermal annealing does not significantly affect the ORR properties of the nondoped CNTs. More importantly, the ORR current density for untreated N-CNTs (Figure 5) is about two times higher than that for the nondoped CNT sample. This is explained by the presence of nitrogen defect sites which act as catalytically active sites for the ORR.[5,9,13,14] Moreover, the thermal annealing of the N-CNTs has a very distinct influence on the ORR properties in contrast to the thermal annealing of the CNTs. The ORR current density is about 1.2 times higher for the N-CNTs treated at 400 °C compared to the untreated N-CNTs accompanied by a positive shift of the peak potential of about 30 mV. The enhanced catalytic efficiency is further expressed for samples treated at higher temperatures. The current density obtains its maximum value for the sample treated at 850 °C but remains almost constant for the sample treated at 1000 °C. For these samples, the current density is 1.7 times higher than the untreated N-CNTs. The large difference in response to the heat treatment for the annealed N-CNTs compared to the annealed CNTs also signals that the iron particles in the samples have negligible contribution to the ORR activity (we note that the iron content and iron particle morphology are similar in N-CNTs and CNTs as evidenced by XPS, TEM, and TGA). This is in some contrast to reports stating that transition metals can take an active role in the ORR processes.[39,40] However, in most of these studies, it is revealed that the active transition metal site is correlated with an Fe−N_x species. In the XPS spectra, Fe−N_x species are characterized by a peak at 397.7 eV. As seen in Figure 2B, no such peak is observed. Another reason for the negligible contribution of the transition metals to the ORR activity can be deduced from the TEM pictures which show that the iron particles adhered on the outside of the N-CNTs and the CNTs all are covered with an amorphous carbon layer (Supporting Information, Figure S3). This carbon layer can efficiently hinder the oxygen to reach the iron particles.

By correlating the ORR measurements with the XPS analysis, we propose that the sharp increase in ORR current density for thermally treated N-CNT samples can be attributed to the increase in N-Q_{valley} sites. The high catalytic ORR efficiency of quaternary nitrogen is in partial agreement with previous reports,[16,41,42] but in neither of these reports have the N-Q_{valley} states been considered or analyzed individually from N-Q_{center}. The very sharp increase in N-Q_{valley} states after thermal treatment as probed by the XPS measurements concurrent with the enhanced catalytic efficiency in these samples implies that the main contribution to the enhanced ORR current density originates from N-Q_{valley} states. The small changes in the evolution of N-Q_{center} sites and pyridinic sites make it more difficult to differ between the ORR activity of N-Q_{center} and pyridinic sites. In previous studies, Kundu *et al.*[13] and Rao *et al.*[14] assigned the largest catalytic ORR efficiency to the pyridinic sites, but it should be noted that in their study the amount of N-Q_{valley} sites is relatively low and therefore not taken into account in their conclusions. The reason that the ORR current density does not increase further for the sample treated at 1000 °C, although the N-Q_{valley} sites continue to increase, is explained by that the overall amount of nitrogen decreases by about 30% for samples treated at 1000 °C so that the total number of available sites is lower.

The total current density obtained in the CV is a combination of several parameters, where the most important are (i) a high turnover frequency (*i.e.*, how

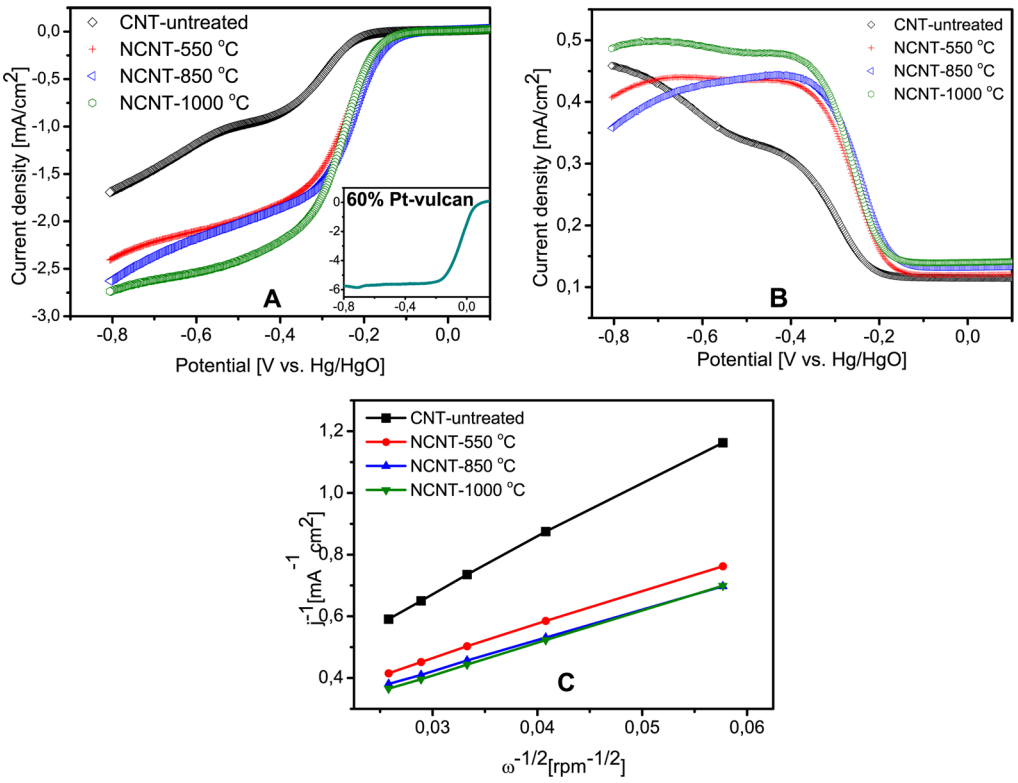

Figure 6. Rotating ring disk electrode voltammograms recorded with CNT, N-CNT-550, N-CNT-850, and N-CNT-1000 electrodes in O_2-saturated 0.1 M KOH at 1500 rpm. (A) Disk current inset: 60% Pt-Vulcan. (B) Ring current. The disk potential was scanned at 10 mV s^{-1}, and the ring potential was constant at 0.6 V. (C) Koutecky–Levich plots of ORR at different potentials on treated N-CNT-modified electrodes.

many catalytic reactions that can occur at a specific site per second), (ii) a high electrical conductivity of the catalyst support in order to conduct electrons to/from the catalytic site, and finally, (iii) the electron transfer number "*n*" which for the ORR process depends on if the oxygen reduction occurs by a direct four-electron pathway to water or by an indirect two-electron pathway *via* hydrogen peroxide, H_2O_2. The general consensus is that the ORR process on nitrogen edge defects (*i.e.*, pyrrolic, pyridinic, and N-Q_{valley} sites) proceeds through the four-electron pathway, while it proceeds *via* the more inefficient two-electron pathway on bulk nitrogen defects, such as the N-Q_{center} sites.[43,44] Many studies have been conducted to study the ORR process of different nitrogen functionalities in nitrogen-containing carbon nanostructures,[44,45] and Gong *et al.*[5] showed that both vertically aligned and nonaligned N-CNTs exhibited efficient catalytic properties with close to four electrons transferred in each step of the ORR.

To get insight into the ORR mechanism of different nitrogen functionalities, different electrodes were prepared for ring disk electrode (RDE) measurements and rotating ring disk electrode (RRDE) measurements. Figure 6A shows the RRDE voltammograms for glassy carbon electrodes modified with CNTs and N-CNTs annealed at 550, 850, and 1000 °C. From Figure 6A, it is clear that the CNT-modified glassy carbon electrode shows a typical feature of a two-electron pathway with two onset potentials of about −0.22 and −0.65 V, similar to the report by Gong *et al.* for nonaligned CNTs, where the first onset is assigned to the two-electron reduction of O_2 to HO_2^-. In contrast, the N-CNTs exhibit clear signs of a direct four-electron process for the ORR similar to the reference Pt-Vulcan sample (inset, Figure 6A) and similar to the N-CNTs studied by Gong *et al.*[5]

The electron transfer number can be calculated in two ways. The first is to use the ring current and the disk current at $V = -0.6$ from Figure 6A,B in eq 2;

$$n = \frac{4I_D}{I_D + \frac{I_R}{N}} \quad (2)$$

where I_D is the Faradaic disk current, I_R is the Faradaic ring current, and $N = 0.4$ is the collection efficiency. The second way to calculate *n* is by using the Koutechy–Levich plots in Figure 6C, which are based on the RRDE current potential curves at different rotation rates for the CNT- and N-CNT-based electrodes (Figure S4, Supporting Information). The transferred electron number *n* can then be calculated by eq 3:[16,46]

$$\frac{1}{j} = \frac{1}{B\omega^{0.5}} + \frac{1}{j_k} \quad (3)$$

where j_k is the kinetic current and ω is the electrode rotating rate. *B* represents the slope of the

curves in Figure 6C:

$$B = 0.2nF(D_O)^{2/3}v^{-1/6}C_O \quad (4)$$

where n represents the number of electrons transferred per oxygen molecule, F is the Faraday constant ($F = 96485$ C mol^{-1}), D_O is the diffusion coefficient of O_2 in 1 M KOH (1.9×10^{-5} cm^2 s^{-1}), v is the kinetic viscosity (0.01 cm^2 s^{-1}), and C_O is the bulk concentration of O_2 (1.2×10^{-6} mol cm^{-3}). The constant 0.2 is adopted when the rotation speed is expressed in rpm. Taking the average of n calculated by the two methods above, measured over three set of samples, gives $n = 1.9 \pm 0.3$, 2.7 ± 0.1, 3.0 ± 0.1, and 2.9 ± 0.2 for the bare CNT, N-CNT-550, N-CNT-850, and N-CNT-1000 electrodes, respectively. It is not unambiguous to interpret the electron transfer number n deduced from our measurements. Taking both the shape of the steady state voltammograms and the deduced electron transfer numbers n into account, it is clear that we go from ORR processes dominated by two-electron pathways for CNTs to ORR processes dominated by four-electron pathways for N-CNTs. However, the thermal annealing of the samples has relatively small effects on the electron transfer numbers, which for all of the annealed samples lie close to three. We rationalize these results in the following way: the rather steep increase in the amount of N-Q_{valley} functionalities is partly compensated by the decrease in pyridinic functionalities and further compensated by a slight increase in the amount of N-Q_{center} functionalities. The almost constant trend for the electron transfer number, n, supports that N-Q_{valley} and pyridinic sites reduce oxygen by a four electron process while the bulk N-Q_{centre} sites reduce oxygen by a two-electron process, in agreement with earlier reports.[43] The fact that the electron transfer numbers are distinctly below three can be explained by two origins: (i) All samples contain a substantial amount of bulk N-Q_{center} sites which contribute only by two-electron pathways and which is evidenced by the rather large evolution of HO_2^- ions seen in the amperometric response curves in Figure 6B. (ii) The nonideal electron transfer from the catalytic sites to the electrodes explained by the fact that the N-CNTs are nonaligned, in contrast to the report by Gong *et al.*, and that the N-CNTs suffer from low dispersibilty resulting in a nonideal film formation.

CONCLUSIONS

We have shown that thermal annealing of nitrogen-doped carbon nanotubes from 500 to 1000 °C allows the transformation of pyrrolic nitrogen functionalities into pyridinic sites followed by a transition to quaternary N-Q_{center} and N-Q_{valley} states. By correlating XPS data with electrochemical measurements, we conclude that certain types of quaternary nitrogen, N-Q_{valley} located at the edge of graphene planes, exhibit the highest catalytic ORR efficiency. RRDE measurements support previous reports that the edge plane nitrogen functionalities N-Q_{valley} and pyridinic sites catalyze four-electron pathways for the ORR process, while bulk N-Q_{center} sites catalyze a two-electron pathway *via* a H_2O_2 intermediate. Our study further improves the understanding of the specific role of nitrogen functionalities for ORR processes and demonstrates a route for transforming low-active sites to high-active states. This will be of importance for the future development of nonmetallic catalyst materials.

METHODS

Synthesis and Treatment. Nondoped and nitrogen-doped CNTs were synthesized by floating catalyst CVD method. A quartz boat containing 10 mg of ferrocene Fe(C_5H_5)$_2$ (Sigma, 98%) was placed in a horizontal quartz tube at the entrance of furnace. Before heating, the system was purged with argon (162 mL/min). When heating the system to 800 °C, the temperature at the entrance reached the evaporation temperature of ferrocene (around 200 °C) which when decomposed to metallic iron constituted the catalyst precursor. Simultaneously, either acetylene (C precursor) or pyridine (C/N precursor) was introduced into the reaction chamber. Acetylene (3.8 mL/min) was carried with the argon flow (162 mL/min), while pyridine was injected into the reaction chamber at different rates using a NEMSYS syringe pump (from Cetoni GmbH) and carried with the same flow of argon. After 45 min of growth, the system was cooled to room temperature and CNTs were collected from the walls of the quartz tube (approximately 30 mg in each run). Four samples were produced at roughly similar conditions containing 3−6% of nitrogen. The samples were divided into six parts that were annealed in argon by loading them in an aluminum oxide crucible and placed at the center of a furnace. The system was purged with argon (162 mL/min), heated to the desired temperature, treated at the predefined time, and then cooled to room temperature.

Characterization. The samples were characterized before and after treatment by various techniques. Transmission electron microscopy (TEM) was performed on a JEOL 1230 transmission electron microscope at 80 keV. XPS was recorded on a Kratos Axis Ultra DLD electron spectrometer using a monochromatic Al Kα source operated at 150 W. Thermogravimetric analyses were measured on a Mettler Toledo TGA/DSC 1 LF/948 at a heating rate 5 °C/min up to 800 °C. The electrocatalytic activity testing of the materials was performed on an Autolab PGSTAT30 with a typical three-electrode cell equipped with gas flow systems at room temperature (about 22 °C).

Electrochemical Testing. A Hg/HgO electrode and a Pt wire were used as reference and counter electrodes, respectively. A glassy carbon electrode coated with N-CNTs or CNTs was used as the working electrode and prepared as follows: (i) 1 mg of N-CNTs or CNTs was mixed with 5 mL of DMF solution containing 10 μL of Nafion solution (5%) and then ultrasonicated for at least 1 h to form a dispersed suspension; (ii) a glassy carbon electrode was carefully polished with 0.05 μm aluminum oxide paste on a chamois and then rinsed subsequently in acetone, ethanol, and water under ultrasonication for 5 min; (iii) 10 μL of suspension mixture was dropped onto the electrode surface (0.07 cm^2) and dried at room temperature in air without any heating process. The obtained electrode was used as the working electrode. One molar KOH was used as the electrolyte solution during the electrochemical measurement. Prior to each measurement, the test solution was bubbled with nitrogen or oxygen for at least 30 min to prepare N_2- or O_2-saturated KOH solution.

For the RDE measurements, catalyst solutions were prepared similar as the method for CV measurement. Fifteen microliter suspensions (0.5 mg/mL) were loaded on a glassy carbon rotating disk electrode of 5 mm in diameter (Pine Instruments). The working electrode was scanned cathodically at a rate of 10 mV s^{-1} with rotating speeds from 300 to 1500 rpm.

For the RRDE measurements, catalyst solutions and electrodes were prepared by the same method as that for RDEs. The suspension was dried slowly in air, and the drying condition was adjusted so that a uniform catalyst distribution across the electrode surface was obtained. The disk electrode was scanned cathodically at a rate of 10 mV s^{-1}, and the ring potential was constant at 0.6 V *vs* Hg/HgO.

Conflict of Interest: The authors declare no competing financial interest.

Acknowledgment. This project was supported by Swedish research council (dnr-2010-3973), Solar Fuels Umeå (Umeå University), Light in Science and Technology Umeå (Umeå University), and the Artificial Leaf Project Umeå (K&A Wallenberg Foundation). T.W. and T.S. thank the JC Kempe Foundation for support. T.W. thanks Åforsk for support. G.Z.H. thanks the Wenner-Gren Foundation for support. Dr. A. Shchukarev is acknowledged for the XPS measurements, and F. Nitze is acknowledged for TGA measurements. Both are acknowledged for valuable discussions.

Supporting Information Available: Complementary TEM pictures, Raman spectra, and RDE current potential curves at different rotation rates for the CNT- and N-CNT-based electrodes. This material is available free of charge *via* the Internet at http://pubs.acs.org.

REFERENCES AND NOTES

1. Zhang, S.; Shao, Y.; Yin, G.; Lin, Y. Carbon Nanotubes Decorated with Pt Nanoparticles *via* Electrostatic Self-Assembly: A Highly Active Oxygen Reduction Electrocatalyst. *J. Mater. Chem.* **2010**, *20*, 2826–2830.
2. Serp, P.; Corrias, M.; Kalck, P. Carbon Nanotubes and Nanofibers in Catalysis. *Appl. Catal. A* **2003**, *253*, 337–358.
3. Wildgoose, G. G.; Banks, C. E.; Compton, R. G. Metal Nanopartictes and Related Materials Supported on Carbon Nanotubes: Methods and Applications. *Small* **2006**, *2*, 182–193.
4. Hu, G. Z.; Nitze, F.; Sharifi, T.; Barzegar, H. R.; Mikolajczuk, A.; Tai, C. W.; Borodzinski, A.; Wågberg, T. Efficient Self-Assembly of Small Size Palladium Nanocrystals on 3D Helical Carbon Nanofibers and Their Excellent Electrocatalytic Performance towards Formic Acid, Ethanol and Methanol in Alkaline Media. *J. Mater. Chem.* **2012**, *22*, 8541–8546.
5. Gong, K.; Du, F.; Xia, Z.; Durstock, M.; Dai, L. Nitrogen-Doped Carbon Nanotube Arrays with High Electrocatalytic Activity for Oxygen Reduction. *Science* **2009**, *323*, 760–764.
6. Shao, Y. Y.; Sui, J. H.; Yin, G. P.; Gao, Y. Z. Nitrogen-Doped Carbon Nanostructures and Their Composites as Catalytic Materials for Proton Exchange Membrane Fuel Cell. *Appl. Catal. B* **2008**, *79*, 89–99.
7. Wong, W. Y.; Daud, W. R. W.; Mohamad, A. B.; Kadhum, A. A. H.; Majlan, E. H.; Loh, K. S. Nitrogen-Containing Carbon Nanotubes as Cathodic Catalysts for Proton Membrane Fuel Cells. *Diamond Relat. Mater.* **2012**, *22*, 12–22.
8. Matter, P. H.; Wang, E.; Arias, M.; Biddinger, E. J.; Ozkan, U. S. Oxygen Reduction Reaction Catalysts Prepared from Acetonitrile Pyrolysis over Alumina-Supported Metal Particles. *J. Phys. Chem. B* **2006**, *110*, 18374–18384.
9. Li, H.; Liu, H.; Jong, Z.; Qu, W.; Geng, D.; Sun, X.; Wang, H. Nitrogen-Doped Carbon Nanotubes with High Activity for Oxygen Reduction in Alkaline Media. *Int. J. Hydrogen Energy* **2011**, *36*, 2258–2265.
10. Kaukonen, M.; Kujala, R.; Kauppinen, E. On the Origin of Oxygen Reduction Reaction at Nitrogen-Doped Carbon Nanotubes: A Computational Study. *J. Phys. Chem. C* **2012**, *116*, 632–636.
11. Chen, Z.; Higgins, D.; Tao, H. S.; Hsu, R. S.; Chen, Z. W. Highly Active Nitrogen-Doped Carbon Nanotubes for Oxygen Reduction Reaction in Fuel Cell Applications. *J. Phys. Chem. C* **2009**, *113*, 21008–21013.
12. Maldonado, S.; Stevenson, K. J. Influence of Nitrogen Doping on Oxygen Reduction Electrocatalysis at Carbon Nanofiber Electrodes. *J. Phys. Chem. B* **2005**, *109*, 4707–4716.
13. Kundu, S.; Nagaiah, T. C.; Xia, W.; Wang, Y.; Dommele, S. V.; Bitter, J. H.; Santa, M.; Grundmeier, G.; Bron, M.; Schuhmann, W.; *et al.* Electrocatalytic Activity and Stability of Nitrogen-Containing Carbon Nanotubes in the Oxygen Reduction Reaction. *J. Phys. Chem. C* **2009**, *113*, 14302–14310.
14. Rao, C. V.; Cabrera, C. R.; Ishikawa, Y. In Search of the Active Site in Nitrogen-Doped Carbon Nanotube Electrodes for the Oxygen Reduction Reaction. *J. Phys. Chem. Lett.* **2010**, *1*, 2622–2627.
15. Niwa, H.; Horiba, K.; Harada, Y.; Oshima, M.; Ikeda, T.; Terakura, K.; Ozaki, J.-i.; Miyata, S. X-ray Absorption Analysis of Nitrogen Contribution to Oxygen Reduction Reaction in Carbon Alloy Cathode Catalysts for Polymer Electrolyte Fuel Cells. *J. Power Sources* **2009**, *187*, 93–97.
16. Lai, L. F.; Potts, J. R.; Zhan, D.; Wang, L.; Poh, C. K.; Tang, C.; Gong, H.; Shen, Z. X.; Lin, J.; Ruoff, R. S. Exploration of the Active Center Structure of Nitrogen-Doped Graphene-Based Catalysts for Oxygen Reduction Reaction. *Energy Environ. Sci.* **2012**, *5*, 7936–7942.
17. Sharifi, T.; Nitze, F.; Berzaghui, H. R.; Tai, C. W.; Mazurkiewicz, M.; Malopeszy, A.; Stobinski, L.; Wågberg, T. Nitrogen Doped Multi Walled Carbon Nanotubes Produced by CVD-Correlating XPS and Raman Spectroscopy for the Study of Nitrogen Inclusion. *Carbon* **2012**, *50*, 3535–3541.
18. Maldonado, S.; Morin, S.; Stevenson, K. J. Structure, Composition, and Chemical Reactivity of Carbon Nanotubes by Selective Nitrogen Doping. *Carbon* **2006**, *44*, 1429–1437.
19. Glerup, M.; Castignolles, M.; Holzinger, M.; Hug, G.; Loiseau, A.; Bernier, P. Synthesis of Highly Nitrogen-Doped Multi-Walled Carbon Nanotubes. *Chem. Commun.* **2003**, 2542–2543.
20. Terrones, M.; Ajayan, P. M.; Banhart, F.; Blase, X.; Carroll, D. L.; Charlier, J. C.; Czerw, R.; Foley, B.; Grobert, N.; Kamalakaran, R.; *et al.* N-Doping and Coalescence of Carbon Nanotubes: Synthesis and Electronic Properties. *Appl. Phys. A: Mater. Sci. Process.* **2002**, *74*, 355–361.
21. Stańczyk, K.; Dziembaj, R.; Piwowarska, Z.; Witkowski, S. Transformation of Nitrogen Structures in Carbonization of Model Compounds Determined by XPS. *Carbon* **1995**, *33*, 1383–1392.
22. Kim, H.; Lee, K.; Woo, S. I.; Jung, Y. On the Mechanism of Enhanced Oxygen Reduction Reaction in Nitrogen-Doped Graphene Nanoribbons. *Phys. Chem. Chem. Phys.* **2011**, *13*, 17505–17510.
23. Pels, J. R.; Kapteijn, F.; Moulijn, J. A.; Zhu, Q.; Thomas, K. M. Evolution of Nitrogen Functionalities in Carbonaceous Materials during Pyrolysis. *Carbon* **1995**, *33*, 1641–1653.
24. Strelko, V.; Kuts, V. The Effect of Nitrogen in the Carbon Matrix on the Donor−Acceptor and Catalytic Activity of Activated Carbons in Electron Transfer Reactions. *Theor. Exp. Chem.* **1999**, *35*, 315–318.
25. Strelko, V. V.; Lavrinenko-Ometsinkaya, Y. D. A Quantum Chemical Study of the Effect of Nitrogen Heteroatoms on the Chemical Parameters of Carbon Sorbents. *J. Mol. Struct.: THEOCHEM* **1989**, *188*, 193–197.
26. Biniak, S.; Szymański, G.; Siedlewski, J.; Świątkoski, A. The Characterization of Activated Carbons with Oxygen and Nitrogen Surface Groups. *Carbon* **1997**, *35*, 1799–1810.
27. Casanovas, J.; Ricart, J. M.; Rubio, J.; Illas, F.; Jiménez-Mateos, J. M. Origin of the Large N 1s Binding Energy in X-ray Photoelectron Spectra of Calcined Carbonaceous Materials. *J. Am. Chem. Soc.* **1996**, *118*, 8071–8076.
28. Wang, W.; Thomas, K. M. The Release of Nitrogen Oxides from Chars Derived from High-Pressure Carbonization of Carbazole and Naphthol during Oxidative Gasification. *Fuel* **1993**, *72*, 293–297.

29. Buckley, A. N. Nitrogen Functionality in Coals and Coal-Tar Pitch Determined by X-ray Photoelectron Spectroscopy. *Fuel Process. Technol.* **1994**, *38*, 165–179.
30. Biddinger, E.; von Deak, D.; Ozkan, U. Nitrogen-Containing Carbon Nanostructures as Oxygen-Reduction Catalysts. *Top. Catal.* **2009**, *52*, 1566–1574.
31. Jiménez Mateos, J. M.; Fierro, J. L. G. X-ray Photoelectron Spectroscopic Study of Petroleum Fuel Cokes. *Surf. Interface Anal.* **1996**, *24*, 223–236.
32. van Dommele, S.; Romero-Izquirdo, A.; Brydson, R.; de Jong, K. P.; Bitter, J. H. Tuning Nitrogen Functionalities in Catalytically Grown Nitrogen-Containing Carbon Nanotubes. *Carbon* **2008**, *46*, 138–148.
33. Matter, P. H.; Zhang, L.; Ozkan, U. S. The Role of Nanostructure in Nitrogen-Containing Carbon Catalysts for the Oxygen Reduction Reaction. *J. Catal.* **2006**, *239*, 83–96.
34. Jacobson, I. A.; Heady, H. H.; Dinneen, G. U. Thermal Reactions of Organic Nitrogen Compounds. I. 1-Methylpyrrole. *J. Phys. Chem.* **1958**, *62*, 1563–1565.
35. Arrigo, R.; Havecker, M.; Schlogl, R.; Su, D. S. Dynamic Surface Rearrangement and Thermal Stability of Nitrogen Functional Groups on Carbon Nanotubes. *Chem. Commun.* **2008**, 4891–4893.
36. Roy, S. S.; Papakonstantinou, P.; Okpalugo, T. I. T.; Murphy, H. Temperature Dependent Evolution of the Local Electronic Structure of Atmospheric Plasma Treated Carbon Nanotubes: Near Edge X-ray Absorption Fine Structure Study. *J. Appl. Phys.* **2006**, 100.
37. Wójtowicz, M. A.; Pels, J. R.; Moulijn, J. A. The Fate of Nitrogen Functionalities in Coal during Pyrolysis and Combustion. *Fuel* **1993**, *72*, 695.
38. Dresselhaus, M. S.; Dresselhaus, G.; Saito, R.; Jorio, A. Raman Spectroscopy of Carbon Nanotubes. *Phys. Rep.* **2005**, *409*, 47–99.
39. Li, Y. G.; Zhou, W.; Wang, H. L.; Xie, L. M.; Liang, Y. Y.; Wei, F.; Idrobo, J. C.; Pennycook, S. J.; Dai, H. J. An Oxygen Reduction Electrocatalyst Based on Carbon Nanotube−Graphene Complexes. *Nat. Nanotechnol.* **2012**, *7*, 394–400.
40. Kramm, U. I.; Herranz, J.; Larouche, N.; Arruda, T. M.; Lefevre, M.; Jaouen, F.; Bogdanoff, P.; Fiechter, S.; Abs-Wurmbach, I.; Mukerjee, S.; *et al.* Structure of the Catalytic Sites in Fe/N/C-Catalysts for O-2-Reduction in PEM Fuel Cells. *Phys. Chem. Chem. Phys.* **2012**, *14*, 11673–11688.
41. Strelko, V. V.; Kuts, V. S.; Thrower, P. A. On the Mechanism of Possible Influence of Heteroatoms of Nitrogen, Boron and Phosphorus in a Carbon Matrix on the Catalytic Activity of Carbons in Electron Transfer Reactions. *Carbon* **2000**, *38*, 1499–1503.
42. Niwa, H.; Horiba, K.; Harada, Y.; Oshima, M.; Ikeda, T.; Terakura, K.; Ozaki, J.; Miyata, S. X-ray Absorption Analysis of Nitrogen Contribution to Oxygen Reduction Reaction in Carbon Alloy Cathode Catalysts for Polymer Electrolyte Fuel Cells. *J. Power Sources* **2009**, *187*, 93–97.
43. Biddinger, E. J.; Ozkan, U. S. Role of Graphitic Edge Plane Exposure in Carbon Nanostructures for Oxygen Reduction Reaction. *J. Phys. Chem. C* **2010**, *114*, 15306–15314.
44. Sidik, R. A.; Anderson, A. B.; Subramanian, N. P.; Kumaraguru, S. P.; Popov, B. N. O-2 Reduction on Graphite and Nitrogen-Doped Graphite: Experiment and Theory. *J. Phys. Chem. B* **2006**, *110*, 1787–1793.
45. Khomenko, V. G.; Barsukov, V. Z.; Katashinskii, A. S. The Catalytic Activity of Conducting Polymers toward Oxygen Reduction. *Electrochim. Acta* **2005**, *50*, 1675–1683.
46. Liang, Y. Y.; Li, Y. G.; Wang, H. L.; Zhou, J. G.; Wang, J.; Regier, T.; Dai, H. J. Co_3O_4 Nanocrystals on Graphene as a Synergistic Catalyst for Oxygen Reduction Reaction. *Nat. Mater.* **2011**, *10*, 780–786.